

NASA/TM-2000-209836



A New Method for Reduction of Photomultiplier Signal-Induced Noise

Andrea Koble
Lund University, Lund, Sweden

Russell DeYoung
Langley Research Center, Hampton, Virginia

January 2000

The NASA STI Program Office . . . in Profile

Since its founding, NASA has been dedicated to the advancement of aeronautics and space science. The NASA Scientific and Technical Information (STI) Program Office plays a key part in helping NASA maintain this important role.

The NASA STI Program Office is operated by Langley Research Center, the lead center for NASA's scientific and technical information. The NASA STI Program Office provides access to the NASA STI Database, the largest collection of aeronautical and space science STI in the world. The Program Office is also NASA's institutional mechanism for disseminating the results of its research and development activities. These results are published by NASA in the NASA STI Report Series, which includes the following report types:

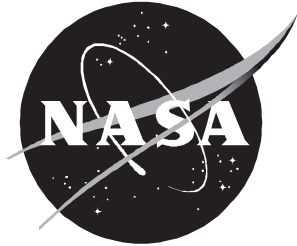
- **TECHNICAL PUBLICATION.** Reports of completed research or a major significant phase of research that present the results of NASA programs and include extensive data or theoretical analysis. Includes compilations of significant scientific and technical data and information deemed to be of continuing reference value. NASA counterpart of peer-reviewed formal professional papers, but having less stringent limitations on manuscript length and extent of graphic presentations.
- **TECHNICAL MEMORANDUM.** Scientific and technical findings that are preliminary or of specialized interest, e.g., quick release reports, working papers, and bibliographies that contain minimal annotation. Does not contain extensive analysis.
- **CONTRACTOR REPORT.** Scientific and technical findings by NASA-sponsored contractors and grantees.
- **CONFERENCE PUBLICATION.** Collected papers from scientific and technical conferences, symposia, seminars, or other meetings sponsored or co-sponsored by NASA.
- **SPECIAL PUBLICATION.** Scientific, technical, or historical information from NASA programs, projects, and missions, often concerned with subjects having substantial public interest.
- **TECHNICAL TRANSLATION.** English-language translations of foreign scientific and technical material pertinent to NASA's mission.

Specialized services that complement the STI Program Office's diverse offerings include creating custom thesauri, building customized databases, organizing and publishing research results . . . even providing videos.

For more information about the NASA STI Program Office, see the following:

- Access the NASA STI Program Home Page at <http://www.sti.nasa.gov>
- Email your question via the Internet to help@sti.nasa.gov
- Fax your question to the NASA STI Help Desk at (301) 621-0134
- Telephone the NASA STI Help Desk at (301) 621-0390
- Write to:
NASA STI Help Desk
NASA Center for AeroSpace Information
7121 Standard Drive
Hanover, MD 21076-1320

NASA/TM-2000-209836



A New Method for Reduction of Photomultiplier Signal-Induced Noise

Andrea Koble
Lund University, Lund, Sweden

Russell DeYoung
Langley Research Center, Hampton, Virginia

National Aeronautics and
Space Administration

Langley Research Center
Hampton, Virginia 23681-2199

January 2000

The use of trademarks or names of manufacturers in this report is for accurate reporting and does not constitute an official endorsement, either expressed or implied, of such products or manufacturers by the National Aeronautics and Space Administration.

Available from:

NASA Center for AeroSpace Information (CASI)
7121 Standard Drive
Hanover, MD 21076-1320
(301) 621-0390

National Technical Information Service (NTIS)
5285 Port Royal Road
Springfield, VA 22161-2171
(703) 605-6000

Contents

- 1. Introduction 1
 - 1.1. Atmospheric Ozone Measurements 1
 - 1.2. Lidar DIAL Ozone Measurement Technique 3
 - 1.3. Lidar Detectors and Signal-Induced Noise 3
 - 1.4. Research Objectives 4
- 2. Theory 4
 - 2.1. DIAL Equation for Ozone 4
 - 2.2. Operation and Theory of Photomultiplier Tubes 6
 - 2.3. Photon-Counting Technique and Theory 7
 - 2.4. Modeling Signal-Induced Noise in Photomultiplier Detectors 8
- 3. Experimental Setup 9
 - 3.1. Signal-Induced Noise Characterization Setup 9
 - 3.2. Simulated LIDAR Signal Setup 10
 - 3.3. Photon-Counting Atmospheric Ozone Measurement Setup 12
- 4. Results and Discussion 14
 - 4.1. Mesh Voltage Reduction of SIN 14
 - 4.2. Mesh Voltage Effect on Simulated Lidar Signal 15
 - 4.3. Mesh Voltage Effect on Simulated Lidar Signal With Addition of SIN 16
 - 4.4. Effect of Mesh Electrode Voltage on Atmospheric Ozone Lidar Returns 17
- 5. Concluding Remarks 19
- 6. References 19

Abstract

For lidar measurements of ozone, photomultiplier tube (PMT) detector signal-induced noise represents a fundamental problem that complicates the extraction of information from lidar data. A new method is developed to significantly reduce signal-induced noise in lidar receiver PMT detectors. The electron optics of the lidar photomultiplier detector is modified to filter the source of signal-induced noise. A mesh electrode external to the PMT is utilized to control photoemission and disorient electron trajectories from the photocathode to the first dynode. Experiments were taken both with simulated and actual lidar return signals at Langley Research Center. Results show at least 40 percent more accurate ozone number density values with a mesh voltage of 60 V applied than with no voltage applied.

1. Introduction

1.1. Atmospheric Ozone Measurements

The distribution of ozone in our atmosphere has been studied for many decades. The first ground-based measurements were conducted in 1956, at Halley Bay, Antarctica. Satellite measurements of ozone started in the early 1970's, but the first comprehensive data came in 1978 with the Nimbus-7 satellite (ref. 1). Data from both ground-based observations and satellites demonstrate a decrease in stratospheric ozone since the 1960's at middle and high latitudes in both the Southern and Northern Hemisphere, and this decrease cannot be explained by known natural processes. In recent years, even an increase in tropospheric ozone has been shown to occur (ref. 2).

Changes in ozone concentration are a major global problem because of its effect on humans and the environment. Because of chemical, dynamical, and radiative processes, ozone as a function of altitude is not evenly distributed in the atmosphere, but approximately 90 percent of all ozone is contained in the stratosphere (the layer between 15 and 50 km above the Earth's surface), as shown in figure 1 (from ref. 3). There it forms a layer that is thinnest in the tropics and denser towards the poles (ref. 4). The location of ozone defines whether it is harmful or beneficial.

Stratospheric ozone is produced by the combination of molecular oxygen and atomic oxygen, the latter being a product of the effect of solar radiation on molecular oxygen. The major production and loss mechanisms are shown as follows:

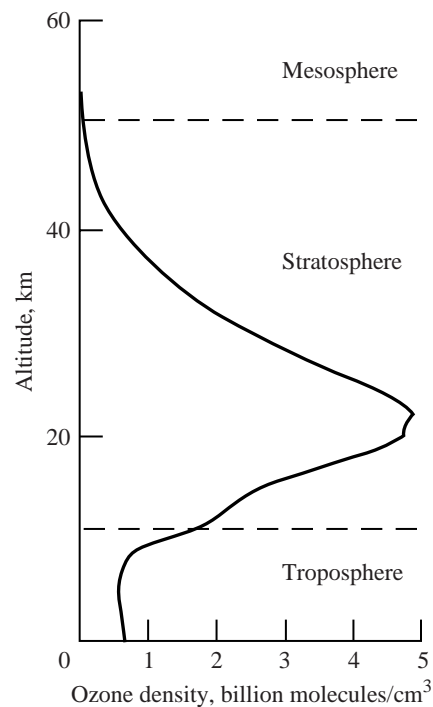
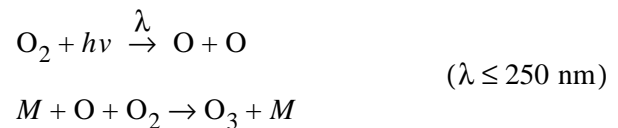


Figure 1. Distribution of ozone in atmosphere as function of altitude. (From ref. 3.)

Production:



Loss:



where

h Planck constant

ν frequency

M any element

λ wavelength, nm

The concentration balance of ozone is controlled by the stratospheric abundance of compounds containing hydrogen, nitrogen, chlorine, and bromine.

Despite its low concentration, stratospheric ozone plays a critical role in chemical and biological processes by absorbing solar ultraviolet radiation in the wavelength range from 220 to 320 nm. The region of concern for biological effects is the ultraviolet-B (UV-B) range from 280 to 320 nm. Depletion of stratospheric ozone leads therefore to an increase of the amount of UV-B reaching the Earth's surface. This depletion can result in damaging effects on humans, like an increase in the incidence of skin cancer and melanoma, genetic changes, eye damage, and also possibly impairing of the human immune system (ref. 5). The increase of UV-B radiation reaching the Earth has also a negative effect on ecological systems and animal life (ref. 6).

Before the early 1970's, no one realized that human activity could harm the ozone layer, but then scientists discovered two potential problems: spray cans and ultrafast passenger aircraft. To achieve fast speeds, the supersonic transport aircraft has to fly high in the atmosphere, where nitrogen in the exhaust could decrease the ozone concentration by enhancing the natural chemical destruction of ozone. The spray cans used aerosol propellants known as chlorofluorocarbons (CFC's), invented in the late 1920's, which contain chlorine, fluorine, and carbon atoms. (See ref. 4.) Although the CFC molecules are heavier than air, they still are present in the stratosphere. The reason is that winds mix the atmosphere to altitudes far above the top of the stratosphere much faster than molecules can settle according to their weight. Gases such as CFC's that are insoluble in water and relatively unreactive in the lower atmosphere are quickly mixed and therefore reach the stratosphere regardless of their weight. At these high altitudes, CFC molecules are broken down

by high-energy solar UV radiation releasing chlorine, which destroys thousands of ozone molecules through a chain reaction. (See ref. 2.) Scientists realized the importance of knowing the level of ozone at different altitudes and the causes for the changes in its concentration and therefore conducted laboratory experiments and launched instrument-carrying balloons into the atmosphere.

In May of 1985, British researchers (ref. 7) reported dramatic declines in ozone concentrations over Antarctica, actual "holes" in the ozone layer. The stratospheric ozone has been shown to be depleted over the last 15 years at certain times of the year over both Antarctica and the Arctic. Ozone levels are measured in Dobson units, which is how thick a layer of ozone would be if all the ozone in the atmosphere was squashed down to the temperature and air pressure at sea level. Dobson units are measured in hundredths of a millimeter, so a measurement of 300 Dobson units corresponds to 3 millimeters of ozone at standard temperature and pressure (STP). Figure 2 shows the lowest recorded ozone levels in a column of air during each year's ozone hole (ref. 8). The data represent the lowest measurement anywhere in the hole, at any time between September 9 and October 10 every year. The ozone concentration in 1993 is shown to be less than 50 percent of the 1979 value. As a direct effect of this phenomenon, the UV-B measured at the surface of the Antarctic can double during the annual ozone hole.

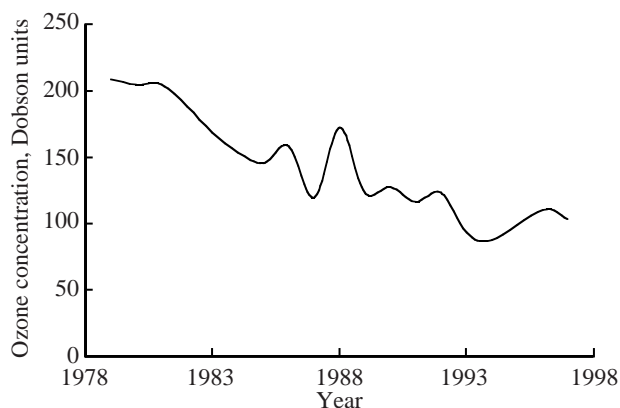


Figure 2. Lowest ozone concentrations over Antarctic between 1979 and 1997 (September 9–October 10).

Figure 3 shows the average size of the hole between September 9 and October 10 of each year. The largest area on a given date was 26 Mkm²

recorded in 1996. It is approximately three times the area of Australia or larger than all of North America. (See ref. 8.)

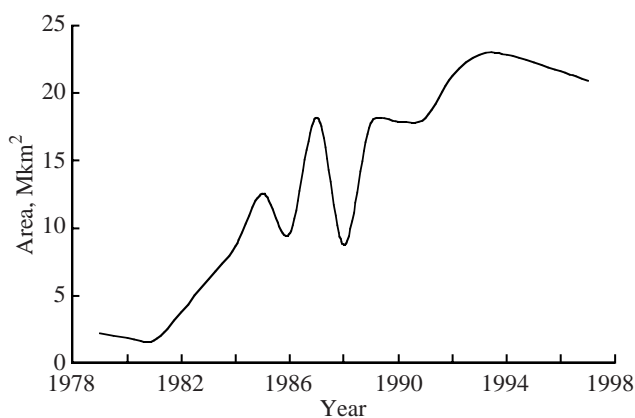


Figure 3. Changes in size of ozone hole over Antarctic between 1979 and 1997 (September 9–October 10).

High ozone levels in the troposphere display a destructive side by causing respiratory problems in humans and lower yields of certain crops and may contribute to global warming. (See ref. 9.) Low-lying ozone is also a key component of smog, a familiar problem in the atmosphere of many cities around the world. It has also been shown that an increase in the tropospheric ozone has a negative effect on agricultural crops (ref. 10), reduces regional forest productivity by significant amounts (ref. 11), and causes transient changes in lung function, respiratory symptoms, and airway inflammation (ref. 12).

Tropospheric ozone arises from two processes: downward flux from the stratosphere and in situ photochemical production from the oxidation of hydrocarbons and carbon monoxide (CO) in the presence of NO_x ($\text{NO} + \text{NO}_2$). Ozone is removed from the troposphere by in situ chemistry and uptake at the Earth's surface. Human impact on the local ozone balance occurs through the emission of precursors, for example, NO_x , CO, and hydrocarbons.

Because of the dramatic changes of ozone in the troposphere and the loss of ozone in the stratosphere, it has become very important to have instruments which can accurately measure the ozone concentrations quickly and at various places around the world. The use of lidar in aircraft can meet this measurement need.

1.2. Lidar DIAL Ozone Measurement Technique

Lidar stands for light detection and ranging and is the optical analogue of radar. The difference is that instead of radio frequency emissions, lidar uses laser radiation, and instead of a dish antenna, lidar uses an optical telescope. Lidars are active remote sensors since they emit the light source on which the measurement depends.

The principle of lidar is based on a laser pulse sent out and reflected by particles and molecules in the atmosphere and detected by a receiver. The altitude of the reflective species is easily determined because the speed of light is known and the time interval between the emission of the pulse and the detection of the back-scattered radiation is measured.

The main components in a lidar system are thus a pulsed laser source, a telescope that collects the back-scattered radiation, and an optical detector that converts the light to an electrical signal.

A special type of lidar called differential absorption lidar (DIAL) is a method for measuring selective atmospheric concentrations, for example, ozone, water vapor, or pollutants. A DIAL system uses two slightly different pulsed laser wavelengths which are selected so that one of the wavelengths is absorbed by the molecule of interest (the “on-line”), whereas the other wavelength is less absorbed (the “off-line”). Comparing the difference in the decay rate of the two return signals, the concentration of the molecule being investigated can be deduced as a function of altitude. This technique is used by NASA to measure ozone concentrations in the troposphere (ref. 13) and stratosphere (ref. 14) at many locations around the world.

1.3. Lidar Detectors and Signal-Induced Noise

In DIAL measurements, the detector usually used to convert the light of the return signals to an electrical signal is a photomultiplier tube (PMT). The photons impinging on the photosensitive cathode surface of the PMT generate photoelectrons, which are amplified inside the tube by means of a dynode chain to finally produce a measurable current pulse at the anode. This output current is assumed to be linearly proportional to the input light intensity. However, if a PMT is

subjected to a high-intensity light pulse, the anode output shows a nonzero residual signal with a slow exponential decay (ref. 15). This phenomenon is called signal-induced noise (SIN) and is the subject of this report.

In DIAL measurements, a high-intensity cloud or near-field return causes the signal-induced noise that alters the real lidar return signal. This problem is especially evident when the light intensities of the return signals are low; that is, the measured concentrations are at a high altitude.

Figure 4 shows a typical lidar return when SIN has corrupted the lidar return signal. In the top of figure 4, a laser pulse is emitted into the atmosphere. At some later time, the PMT gate opens allowing the PMT to measure the signal return from the atmosphere. The bottom of figure 4 shows that even when the PMT is gated off, there still is a very intense atmospheric light signal hitting the PMT photocathode. When the PMT gate opens, the signal actually measured is a combination of the atmospheric lidar return and a noise signal caused by the near-field light saturation of the PMT. This noise signal (SIN) tends to lengthen the decay of the lidar signal to be measured; this results in an incorrect ozone measurement.

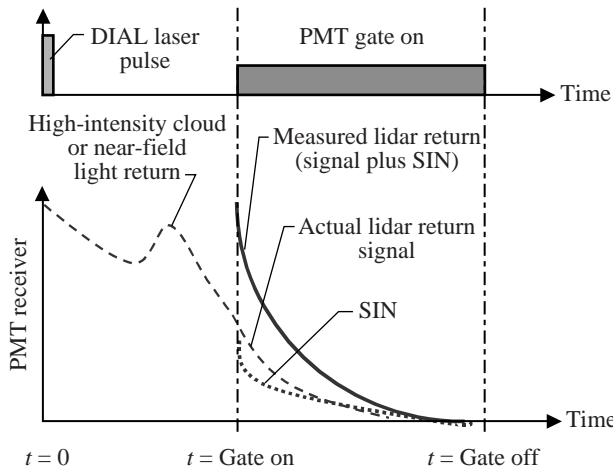


Figure 4. Formation of measured lidar signal by addition of SIN to actual lidar return.

Some researchers tried to subtract the signal-induced noise by different modeling methods (ref. 16), but the complexity of the data analysis increased and the validity of the values was uncertain. Other methods used a mechanical chopper to block the incoming

near-field intense light pulse (ref. 17), but such methods require extremely fast, heavy, and cumbersome mechanical choppers. NASA researchers utilized a metal ring external to the PMT to control photoemission (ref. 18).

1.4. Research Objectives

Because it is difficult to determine the PMT baseline due to the addition of signal-induced noise to the lidar return signal, reducing SIN is desirable in the DIAL receiver. A reduction of the signal-induced noise would permit more valid ozone density measurements at much greater altitude ranges.

This report discusses the neutralization of the SIN effect by means of a pulsed external electric field placed in front of the PMT DIAL detector. This field distorts the electron trajectories during the intense near-field light pulse, which does not allow the electrons to be amplified by the dynode chain when the PMT gate opens at a later time.

First, the optimum conditions for reduced signal-induced noise are determined through analysis of data obtained through laboratory research with simulated SIN decays. After this, the effect of the electrode voltage on the time constant of a simulated lidar return is examined because this is very important in achieving valid ozone density measurements. As an attempt to explain the changes the external electric field is causing inside the PMT, a simulation program is used to depict the effect of this electric field. Finally, real ground-based ozone DIAL measurements are conducted to determine the effect of the electrode potential on actual ozone lidar returns and quantify the degree of measurement improvement.

2. Theory

2.1. DIAL Equation for Ozone

When conducting ozone measurements, it is possible to predict the lidar return signal by using the so-called lidar equation. In this type of measurement, the scattering form of the equation is used, and it gives the expected received power from the elastic backscattering of a laser pulse propagated into the atmosphere.

The lidar equation (eq. (1)), relates the power received $P_r(\lambda, R)$ to the optical receiver and atmospheric parameters (ref. 19):

$$P_r(\lambda, R) = \frac{P_0 F(\lambda, R) c \tau_L}{R^2} \frac{1}{2} \beta(\lambda, R) \times \exp \left[-2 \int_0^R \kappa(\lambda, R) dR \right] \quad (1)$$

where

P_0 initial power of laser pulse

R range between telescope and atmospheric target

$F(\lambda, R)$ function that depends on receiver's spectral transmission factor and also includes a geometrical form factor

c speed of light

τ_L duration of laser pulse

$\beta(\lambda, R)$ volume backscattering coefficient

$\kappa(\lambda, R)$ total extinction factor including all scattering and absorption losses at laser wavelength

Lidar measurements can only give the relative distribution of molecules or particles in the atmosphere. In order to determine the number density of a particular species, such as ozone, the DIAL technique can be used. This technique involves two laser pulses: the on-line at 300 nm having stronger ozone absorption than the off-line wavelength at 311 nm. These wavelengths and the ozone absorption cross section are shown in figure 5 (data from ref. 20).

Both wavelengths are subjected to the same scattering and absorption processes, since they have the same trajectory in the atmosphere. Because of the difference at the two wavelengths in the absorption coefficient for the target media, there is a difference in the return signals. By taking the ratio between these signals, for example, equation (1) with the different λ_{on} and λ_{off} , we obtain the DIAL equation:

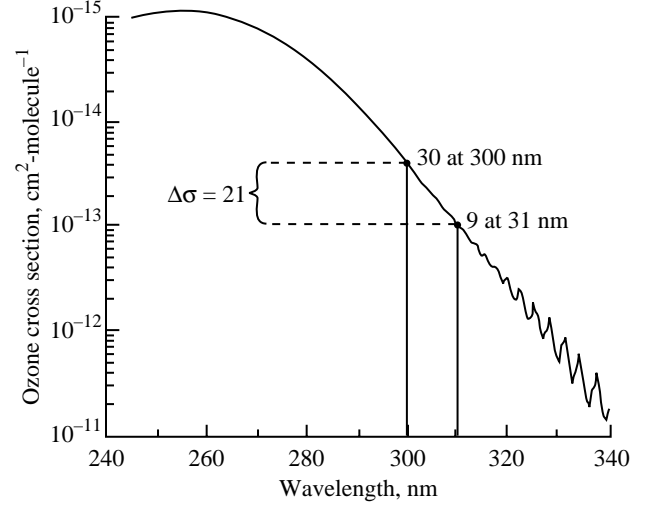


Figure 5. Ozone absorption cross section versus wavelength. (Data from ref. 20.)

$$\frac{P(\lambda_{\text{on}}, R)}{P(\lambda_{\text{off}}, R)} = \frac{\beta(\lambda_{\text{on}}, R)}{\beta(\lambda_{\text{off}}, R)} \times \exp \left\{ -2 \int_0^R [\kappa(\lambda_{\text{on}}, R) - \kappa(\lambda_{\text{off}}, R)] dR \right\} \quad (2)$$

When taking a ratio, most terms cancel each other except the volume backscattering and the total extinction coefficients. Keeping the exponential factor on one side by itself and taking the natural logarithm of both sides give

$$\ln \left[\frac{P(\lambda_{\text{on}}, R) \beta(\lambda_{\text{off}}, R)}{P(\lambda_{\text{off}}, R) \beta(\lambda_{\text{on}}, R)} \right] = -2 \int_0^R [\kappa(\lambda_{\text{on}}, R) - \kappa(\lambda_{\text{off}}, R)] dR \quad (3)$$

Expressing the total extinction coefficient as a sum of the coefficient of absorption and extinction due to aerosols κ_a and the product of the ozone absorption cross section $\sigma(\lambda)$ and the ozone number density $N(R)$ is possible as follows:

$$\kappa(\lambda, R) = \kappa_a(\lambda, R) + \sigma(\lambda) N(R) \quad (4)$$

Inserting equation (4) into equation (3) and taking the derivative of both sides gives

$$\begin{aligned}
& \frac{d}{dR} \ln \left[\frac{P(\lambda_{\text{on}}, R)}{P(\lambda_{\text{off}}, R)} \frac{\beta(\lambda_{\text{off}}, R)}{\beta(\lambda_{\text{on}}, R)} \right] \\
&= -2 \{ [\kappa_a(\lambda_{\text{on}}, R) + \sigma(\lambda_{\text{on}}) N(R)] \\
&\quad - [\kappa_a(\lambda_{\text{off}}, R) + \sigma(\lambda_{\text{off}}) N(R)] \} \quad (5)
\end{aligned}$$

Solving for $N(R)$ results in

$$\begin{aligned}
N(R) &= - \frac{1}{2[\sigma(\lambda_{\text{on}}) - \sigma(\lambda_{\text{off}})]} \\
&\quad \times \frac{d}{dR} \ln \left[\frac{P(\lambda_{\text{on}}, R)}{P(\lambda_{\text{off}}, R)} \frac{\beta(\lambda_{\text{off}}, R)}{\beta(\lambda_{\text{on}}, R)} \right] \\
&\quad - \frac{\kappa_a(\lambda_{\text{on}}, R) - \kappa_a(\lambda_{\text{off}}, R)}{[\sigma(\lambda_{\text{on}}) - \sigma(\lambda_{\text{off}})]} \quad (6)
\end{aligned}$$

In order to simplify equation (6), the following differential absorption cross section is introduced, as shown in figure 5:

$$\Delta\sigma = \sigma(\lambda_{\text{on}}) - \sigma(\lambda_{\text{off}}) \quad (7)$$

and both the volume backscattering coefficient β and the attenuation coefficient κ are assumed to be independent of wavelength over this small wavelength interval. This simplification gives the following equation:

$$N(R) = - \frac{1}{2 \Delta\sigma} \frac{d}{dR} \ln \left[\frac{P(\lambda_{\text{on}}, R)}{P(\lambda_{\text{off}}, R)} \right] \quad (8)$$

If dR is assumed very small, an approximation can be used for the derivation, which gives the following final form of the DIAL equation over a range cell $\Delta R = (R_2 - R_1)$:

$$N(R) = - \frac{1}{2 \Delta\sigma \Delta R} \ln \left[\frac{P(\lambda_{\text{off}}, R_2) P(\lambda_{\text{on}}, R_1)}{P(\lambda_{\text{off}}, R_1) P(\lambda_{\text{off}}, R_2)} \right] \quad (9)$$

This form of the DIAL equation is used to determine ozone concentrations from the measured lidar returns. Because it is a fairly simple system but also easily mobile, the DIAL technique can be used from trucks (ref. 21), aircraft, or even on a space shuttle (ref. 22).

2.2. Operation and Theory of Photomultiplier Tubes

Photomultiplier tubes are sensitive light detectors that are useful in low-intensity light applications. They consist of a photocathode and a series of dynodes in an evacuated glass enclosure as shown in figure 6 (from ref. 23). Photons that strike the photosensitive cathode emit electrons due to the photoelectric effect. The electrons are focused by a high electric field and accelerated towards a series of dynodes maintained at a more positive potential. Additional electrons are generated at each dynode resulting in a cascading effect that creates 10^5 to 10^7 electrons for each photon hitting the first dynode, depending on the number of dynodes and the accelerating voltage. This amplified signal is finally collected at the anode where it can be measured. (See refs. 24 and 25.)

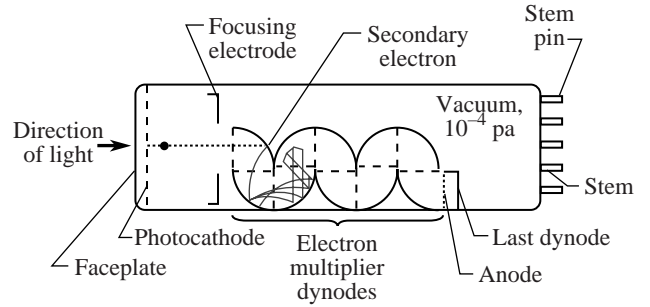


Figure 6. Schematic of typical PMT. (From ref. 23.)

An important characteristic of the photocathode of the PMT is the quantum efficiency, a probability defined as the number of photoelectrons emitted by the photocathode divided by the number of incident photons. The higher the quantum efficiency, the more efficient the PMT detector is at a given wavelength.

Some other key characteristics of PMT's are gain, dark current, signal-to-noise ratio, and signal-induced noise. The gain is expressed as the ratio of the output signal current to the photoelectric signal current from the photocathode (ref. 26) and depends on the secondary electron emission coefficients of the dynodes involved.

The dark current is the small amount of current that flows in a photomultiplier tube even when no

incident light is present. There are several causes for this phenomenon, the most important being (ref. 27)

Thermionic emission current from the photocathode and the dynodes

Leakage between the anode and other electrodes inside the tube

Photocurrent produced by scintillation glass envelope or electrode supports

Ionization current from residual gases

Noise current caused by cosmic rays, radiation from radioisotopes, and environmental gamma rays

Signal-induced noise produced in PMT's is now discussed. One way to understand how much noise a system has is to look at the signal-to-noise ratio (SNR) defined as the ratio of the pulses from the signal to be measured to the total noise. To obtain a better SNR, one has to use a PMT that has a high quantum efficiency in the wavelength range to be measured and to design the system for better light collection efficiency so that the incident light is guided to the photomultiplier tube with minimum loss (ref. 27).

2.3. Photon-Counting Technique and Theory

Two ways of processing the output signal of a PMT are using either analog or digital technique,

depending on the incident light intensity. The analog case is applied at high light intensities and high signal-to-noise ratios. Usually, the anode output is conducted through a resistor that transforms the anode current into an average voltage, after which the voltage signal is amplified and processed for computer analysis.

If the light level becomes very low, the output signal is discrete light pulses (single photons) that can be discriminated and counted in a digital mode. A typical schematic configuration for a photon-counting system is shown in figure 7. In this system, the voltage output pulses from the PMT are amplified and fed to a discriminator that separates the signal pulses from the noise pulses to enable high-precision measurement with a higher signal-to-noise ratio in comparison with the analog mode (ref. 27). All pulses higher than a preset threshold voltage are shaped as equal height and width pulses and sent next to a digital counter composed of a multichannel scaler (MCS) with an averaging memory. Each channel stores the number of pulses received from the discriminator during an interval of time determined by the system clock and the final distribution is sent to a computer.

The photon-counting system has three main noise sources: background light, dark current, and signal light. An expression of the signal-to-noise ratio in the system is given by the following equation (ref. 26):

$$SNR = \frac{N_s \sqrt{T}}{\sqrt{N_s + 2(N_b + N_d)}} \quad (10)$$

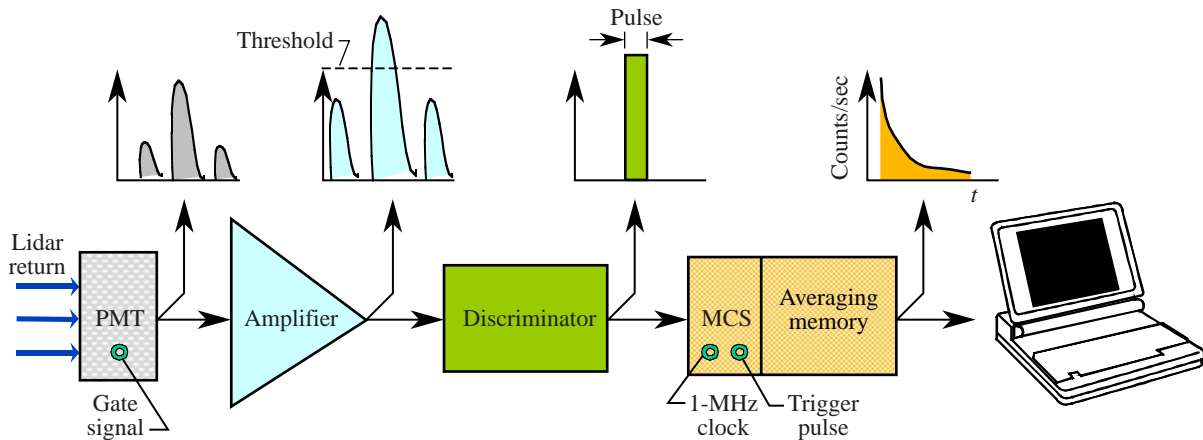


Figure 7. Photon-counting schematic.

where

N_s	number of counts per second resulting from incident light signal
N_b	number of counts per second resulting from background light
N_d	number of counts per second resulting from dark current
T	measurement time

Equation (10) shows that SNR for the photon counting mode increases as the square root of the measurement time. Hence, by counting for long times, extremely low signals can be detected, which would otherwise be lost in the analog mode of detection.

2.4. Modeling Signal-Induced Noise in Photomultiplier Detectors

In the 1970's, the output of a PMT was noticed to have a tail (nonzero baseline) after a short high-intensity pulse signal was received (ref. 28). The high-intensity pulse, that could be a near-field or high-intensity cloud lidar return, saturates the PMT and causes a slowly decaying noise signal. This noise signal, known as signal-induced noise, can be significant in that it can change the atmospheric decay signal in the DIAL measurement because of both its magnitude as well as its long decay, as discussed in section 1.3.

Applying an electrical field to a conductor placed against the photocathode of the photomultiplier affects

the anode signal (ref. 29). With this idea, the goal of this report is to show that signal-induced noise can be reduced by placing a mesh electrode external to the PMT. The purpose of this mesh is to change the electron optics of the PMT: to control photoemission and disorient electron trajectories from the photocathode to the first dynode. This technique could result in less SIN being measured during the time the PMT is gated on.

A simplified PMT schematic with an external mesh electrode can be seen in figure 8. Through the photoelectric effect, light impinging on the photocathode releases electrons that move towards the first dynode. By applying a positive voltage to the mesh, the electric field inside the PMT is changed. Thus electrons with low kinetic energy are injected back into the photocathode, whereas those that have higher energies have disoriented trajectories to the first dynode or the insulator surfaces. If the positive voltage is applied to the mesh when the high-intensity near-field light hits the photocathode, the electrons do not travel to the dynodes when the PMT gate opens and the PMT does not experience signal-induced noise.

For a better understanding of how the signal-induced noise phenomenon is affected by the electrode mesh, a simulation program was used. SIMION 3D (ref. 30) is a C-based program that can model complex problems by using an ion optics workbench with electrostatic and magnetic potential arrays. The ion trajectories and potential energy surfaces can be inspected, analyzed, and changed during the simulation.

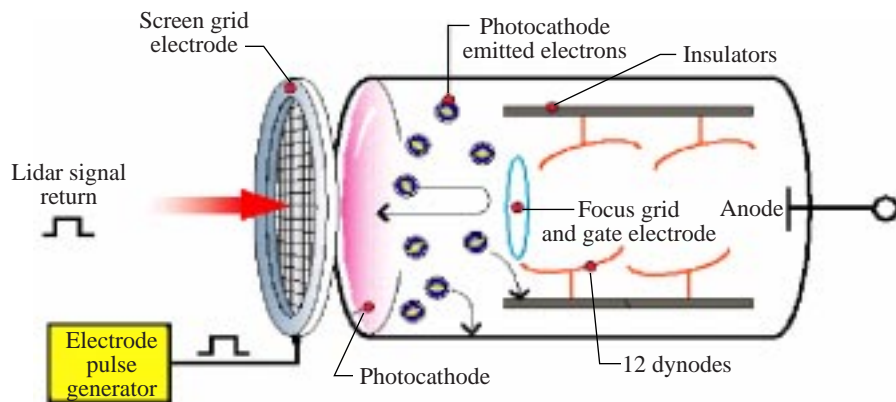


Figure 8. Signal-induced noise suppression system.

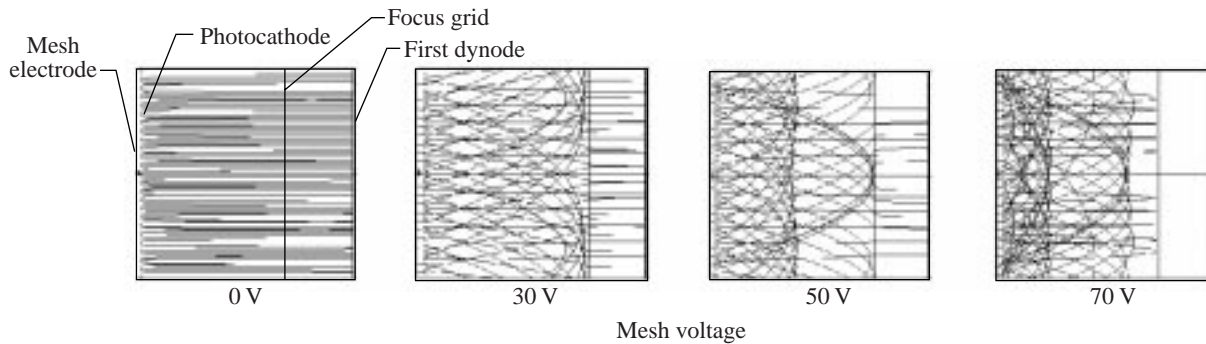


Figure 9. SIMION simulation of effect of mesh electrode on PMT electron trajectories.

The PMT configuration (from external mesh electrode to the first dynode only) was approximated by flat surfaces but with the same proportions as the PMT. In the simulations, as well as during the experiments, the PMT was gated off, which means that the focus grid voltage and the photocathode voltage were both 0 V, whereas the first dynode voltage was 300 V. In addition to this, the mesh voltage was varied between 0 and 80 V.

The kinetic energy of the emitted electrons was set to 1 eV, according to reference 24. The result of how the electron trajectories change when the mesh voltage is varied can be seen in figure 9. In this configuration, the first surface is the external mesh electrode, the second one in close proximity is the photocathode (dashed-line surface that allows the electric field from the mesh to penetrate), and the last two surfaces represent the focus grid and the first dynode.

The lines in figure 9 represent the electron trajectories; the higher the voltage on the mesh, the fewer electrons get to the first dynode. Applying this voltage to the electrons that cause the SIN would eliminate this effect. According to this model, applying a voltage of 60 V on the mesh electrode reduces the SIN effect by 80 percent, as seen in figure 10.

According to this fairly simple theoretical approximation, we could reduce the SIN effect by 80 percent with a mesh voltage of 50 to 60 V. In reality, the dark current, thermionic emissions, and other effects will be present and cause a current at the anode. Therefore, we should not expect a 100-percent reduction of the signal-induced noise effect either.

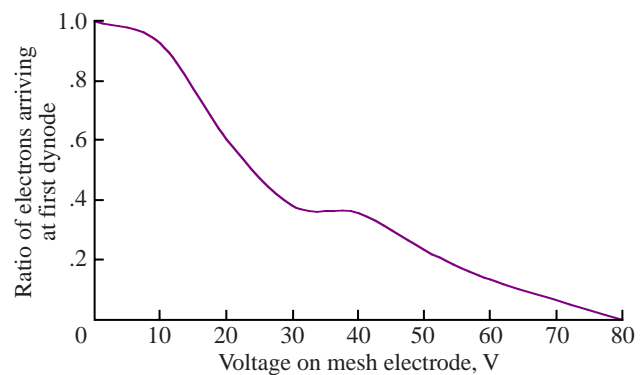


Figure 10. Effect of electrode mesh on SIN in SIMION simulation.

These results are verified in the experiments in the following discussions. By simulating a signal-induced noise signal and applying an electric field on the external mesh electrode of the same order as in the theoretical approximation, it is possible to see how accurate these results are.

3. Experimental Setup

3.1. Signal-Induced Noise Characterization Setup

The first experimental setup (fig. 11) was used to examine the effect of the mesh electrode on signal-induced noise. The light source causing the SIN consisted of a blue light emitting diode (LED) placed in front of the PMT. By adding neutral density (ND) filters between the LED and the photocathode of the PMT, the intensity of the light pulse could be easily varied. The PMT used was an Electron Tubes model 9214QMA, and the signal from its anode was

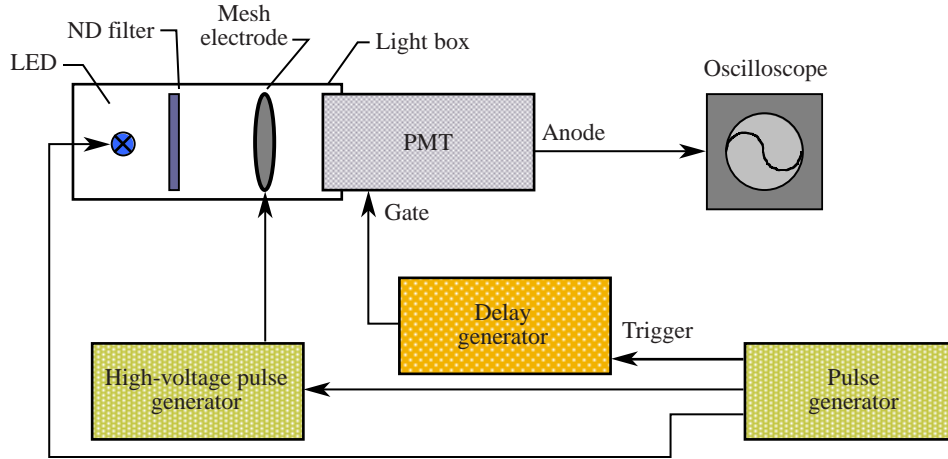


Figure 11. Experimental setup for examining mesh electrode effect on SIN.

connected to an oscilloscope (50Ω termination) where it could be observed and analyzed.

The pulse generator turned on the LED to create a high-intensity light pulse to saturate the PMT. It also transmitted a pulse to the high-voltage pulse generator which sent voltage pulses from 0 to 100 V to the mesh electrode. A trigger from the pulse generator was sent to a delay generator that after a variable delay turned on the PMT gate circuit, which allowed the PMT output to be measured. The timing diagram is shown in figure 12. The length and the amplitude of the pulses were easily varied, as well as the time interval between them. When the PMT was gated off, no signal was recorded at the anode. During the “gate-on” time,

the anode receives the signal-induced noise caused by the high-intensity LED pulse. As shown in figure 12, the voltage pulse on the mesh is aimed to be superimposed on the LED pulse, whereas the gate opens after a variable time interval Δt controlled by the delay generator. The amplitude and the decay constant of the SIN signal were finally observed on the oscilloscope.

The mesh electrode (fig. 13) consists of a quartz glass window on which a gold foil grid was deposited. The lines in the grid are $50 \mu\text{m}$ wide and the spacing between them is 2 mm; thus, the photons can travel through to the PMT. The light attenuation of the grid was measured and found to be a 20-percent loss. The PMT glass surface is located 2 mm from the mesh.

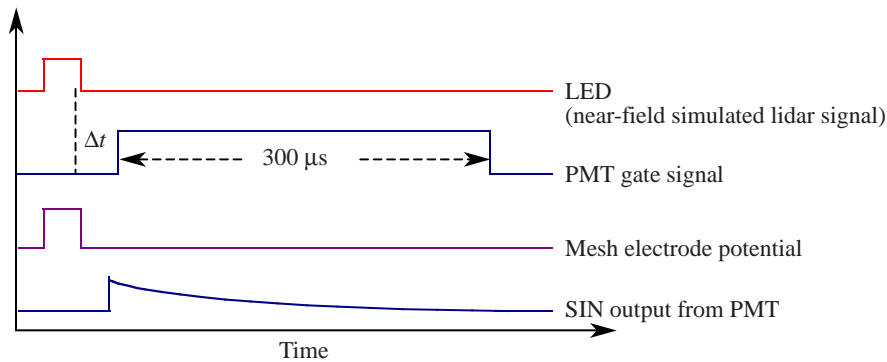


Figure 12. Timing diagram for analysis of SIN.

3.2. Simulated LIDAR Signal Setup

Knowing if the mesh electrode voltage affects the actual lidar return signal in any way is very important, since this would lead to changes in the results of the ozone number density. The experimental setup to sim-

ulate a lidar return on the PMT can be seen in figure 14, and the corresponding timing diagram is shown in figure 15. This setup is basically the same as the setup for SIN characterization, except that a second LED (LED 2) and a function generator were added.

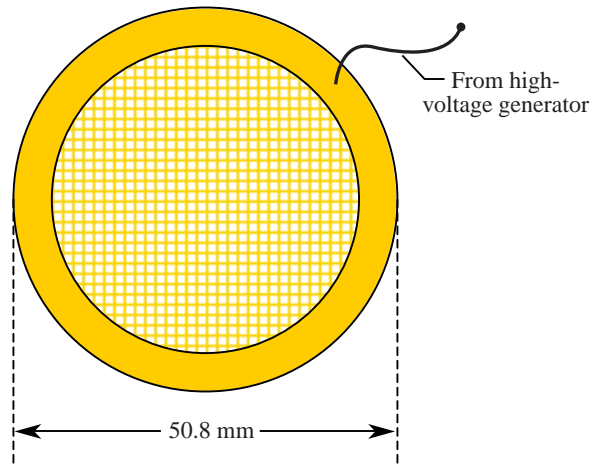


Figure 13. Mesh electrode used in front of PMT photocathode.

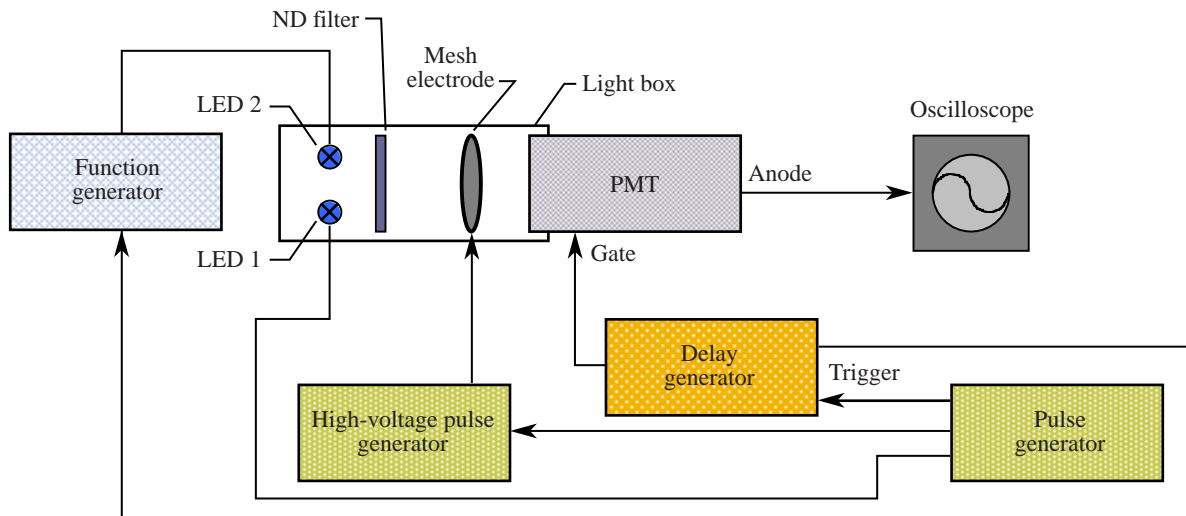


Figure 14. Experimental setup for simulation of lidar return signal and characterization of signal-induced noise.

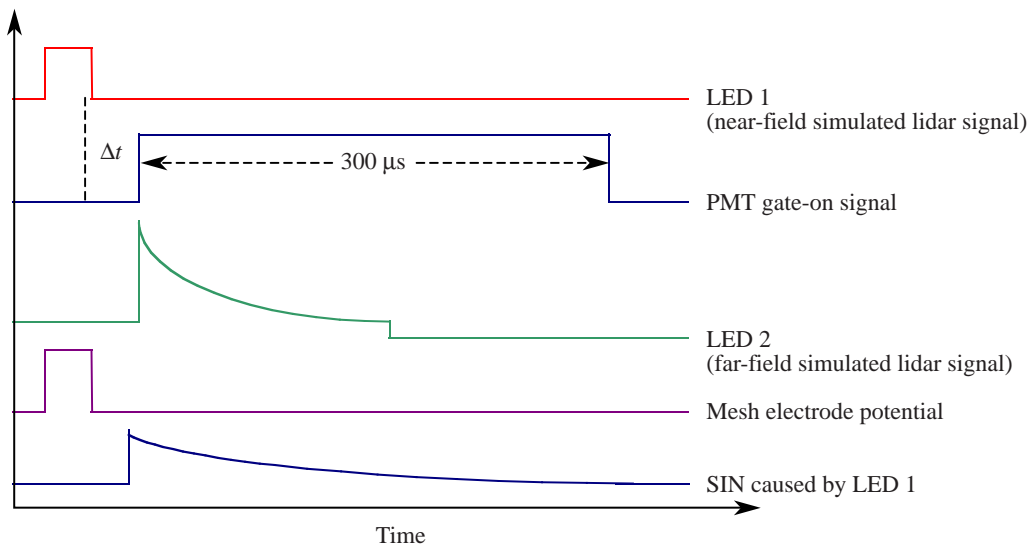


Figure 15. Timing diagram for simulation of lidar returns.

In this experimental setup, the pulse generator would first turn on the mesh electrode voltage and LED 1 to saturate the PMT photocathode. At some delayed time, the delay generator would turn on the PMT gate allowing the PMT to measure input light. The function generator, triggered by the pulse generator, creates a simulated far-field lidar return pulse on LED 2, which starts just as the PMT gate opens. The function generator was programmed to provide a decaying exponential pulse to LED 2 at a fixed time constant. By looking at the amplitude and the time constant of the anode output, it is possible to determine whether the change in the electric field due to the mesh electrode induces any alteration of the simulated far-field lidar return signal.

3.3. Photon-Counting Atmospheric Ozone Measurement Setup

The DIAL system currently used at the Langley Research Center is depicted in figure 16. This experimental setup was used to measure actual ozone returns and determine the effect of the mesh voltage on off- and on-line decays. Two frequency-doubled Nd:YAG lasers are used to pump two high-conversion efficiency tunable dye lasers. All four lasers were mounted on a rigid support structure that also supports

all the laser power supplies, the laser beam transmitting optics, and the dual telescope and detector packages for simultaneous nadir and zenith O_3 and aerosol measurements. The output of the dye lasers was doubled and results in laser operation at 289 and 299 nm for tropospheric measurements or 301 and 311 nm for stratospheric measurement for on-line and off-line, respectively. The DIAL wavelengths are produced in sequential pulses with a time separation of 300 μs to ensure that the same atmospheric scattering volume is sampled at both wavelengths. The repetition rate of the lasers is 30 Hz, the pulse lengths are 8 to 12 ns, and the output energy is usually 15 to 30 mJ. When operated on an aircraft, half of each UV beam is transmitted in the zenith and nadir directions, whereas for ground-based measurements the laser beams are transmitted in the zenith through an opening in the building ceiling (refs. 22 and 31).

The receiver for this research effort consisted of a 35.5-cm-diameter parabolic mirror, shown as the fiber-optic coupled receiver system in figure 16. A fiber was fed to a lens that collimated the light and sent it through a narrowband optical filter as shown in figure 17. Next, the light passes the mesh electrode and reaches the PMT photocathode. For the DIAL

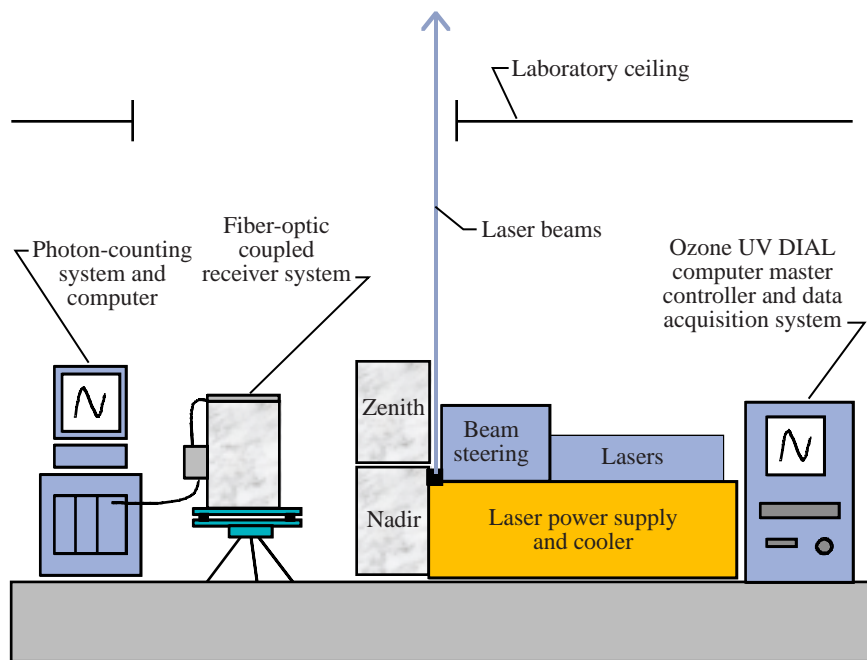


Figure 16. Ozone UV DIAL system for ground-based measurements at Langley Research Center. (From ref. 33.)

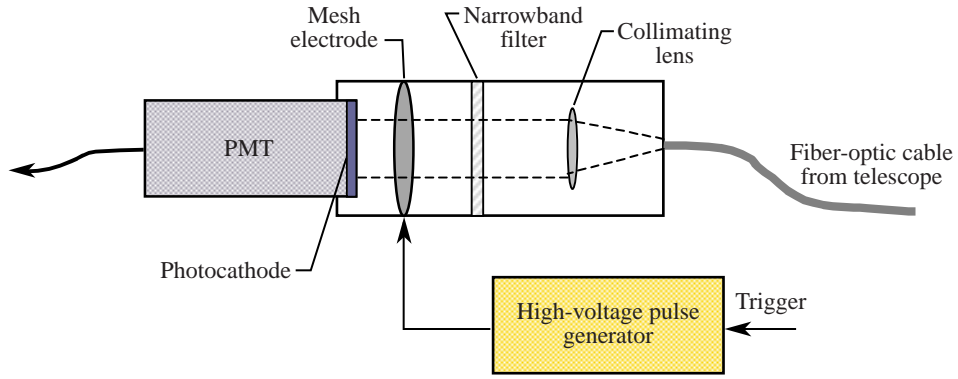


Figure 17. Path of lidar return from receiver system to photon-counting setup.

measurements, the PMT model used was an Electron Tubes model 9214Q, serial 5150, with a bialkali Sb-K-Cs photocathode material, a quantum efficiency of 24 percent at 300 nm, and an operating voltage of -1200 V. Its gain is approximately 8×10^6 at this voltage (ref. 32).

The signal from the PMT was directed into a photon-counting system represented in figure 18. The first element is a 300-MHz amplifier with a gain of 5 and an input impedance of 50Ω . The amplified signal

is then sent to a 300-MHz discriminator with the threshold usually set to 150 mV. (See also fig. 7.) A multichannel scaler receives the pulses above the threshold, counts, and stores them into time bins. A 1-MHz clock rate, provided by the UV DIAL transmitter master controller, gives a count time of $1 \mu\text{s}/\text{bin}$. The number of pulses in each bin is stored in an averaging memory.

A computer automated measurement and control (CAMAC) crate holds the discriminator, the MCS,

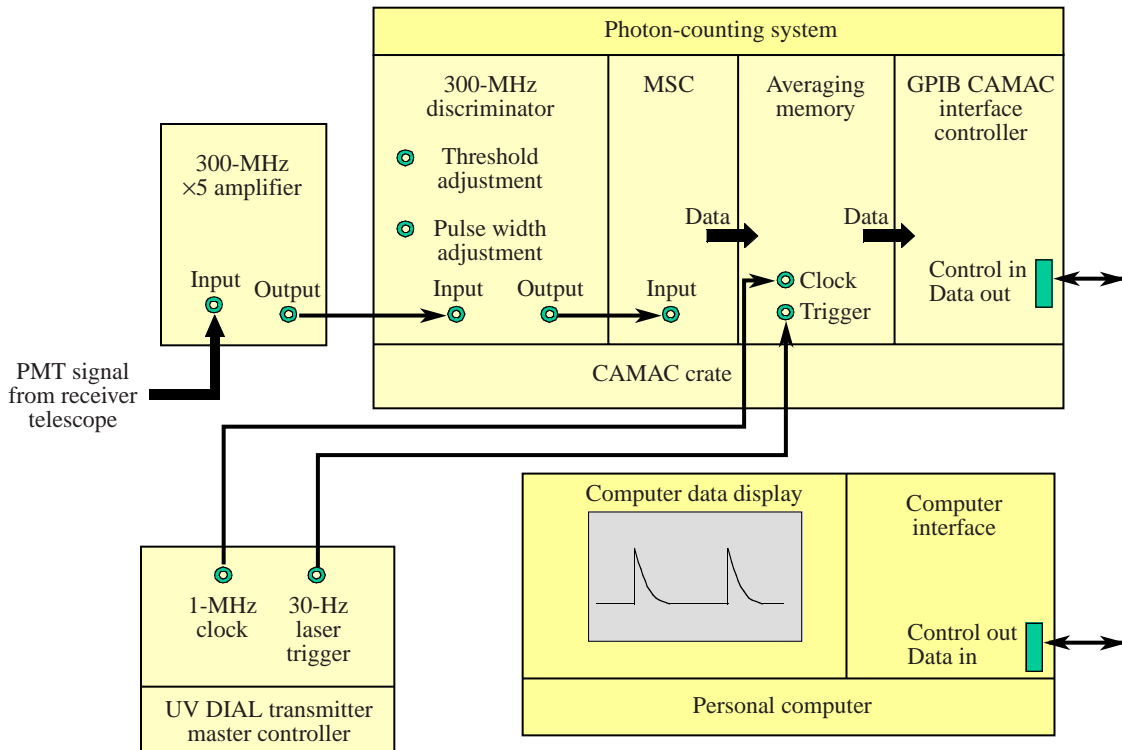


Figure 18. Photon-counting system setup. (From ref. 33.)

and the averaging memory together with a GPIB CAMAC crate controller that allows computer interface with the mounted components. Finally, the computer uses a specially developed software program (ref. 33) through which data are recorded into files and displayed on the monitor. The files can easily be converted to text files to allow a convenient form of analyzing the return signals.

4. Results and Discussion

4.1. Mesh Voltage Reduction of SIN

The theoretical SIMION modeling of the PMT configuration showed that the mesh electrode significantly affects the signal-induced noise as discussed in section 2.4. In this section, the experimental setup shown in figure 11 was used with the related timing diagram of figure 12 to find out whether the same result was obtained experimentally. The SIN signal was measured at the time the PMT gate opened.

The voltage on the mesh electrode was varied between 0 and 80 V in steps of 10 V, and the SIN signal from the PMT was recorded on a photon-counting system. The width of the high-intensity LED signal (the cause of the SIN) was 10 μ s, the same as the delay Δt between the end of the LED pulse and the PMT gate opening. Changing the neutral density varied the intensity of the saturating LED pulse. The PMT was saturated when the ND light transmission was 0.001, that is an ND factor of 3 (Transmission = 10^{-ND}). Thus, decreasing the ND factor by 1.0 increased the light intensity by a factor of 10. The result of the measurement can be seen in figure 19. In this graph, the SIN reduction factor was defined as

$$RF = \frac{\text{SIN signal with voltage on mesh electrode}}{\text{SIN signal with no voltage on mesh electrode}} \quad (11)$$

Comparing the experimental results with that of the theoretical SIMION simulation (dashed curve in fig. 19) shows that the shapes of the graphs are nearly the same. Although the number of electrons arriving at the first dynode in the SIMION simulation goes to zero as electrode voltage increases, a point is reached in the laboratory experiments where the reduction factor does not go lower than 0.2. This difference suggest

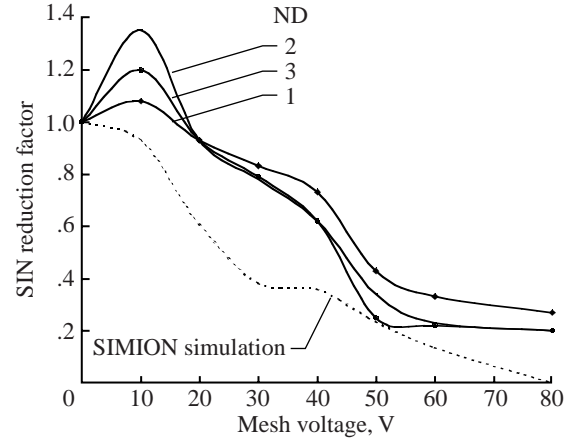


Figure 19. Effect of mesh voltage on signal-induced noise at different PMT saturation levels.

that the mesh voltage is not completely effective in capturing all electrons created during the intense light saturating pulse, due to the shielding effect of the electron cloud near the PMT photocathode.

Figure 19 shows only what happens with the peak of the SIN signal, that is, the value of the SIN signal when the PMT gate just opens. To see what happens later, measurements were taken at two additional times after the PMT gate opened. A neutral density of 2 was used, which gave a $\times 10$ PMT saturation level. The SIN level was not only observed at the peak of the signal but also at 50 and 100 μ s after the gate opened. The results depicted in figure 20 show that the reduction of SIN occurs throughout the whole signal.

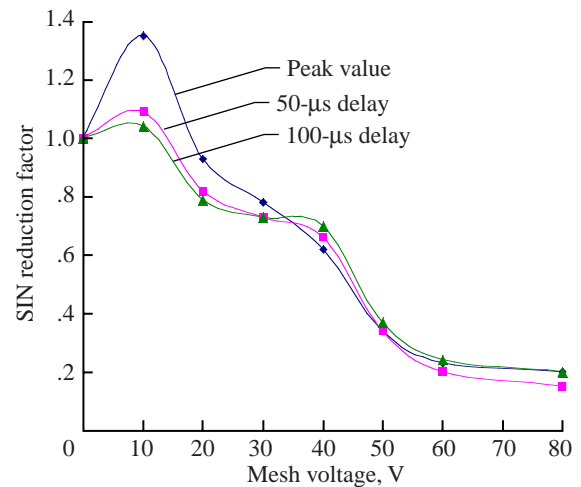


Figure 20. Effect of mesh voltage on signal-induced noise at different delay times after PMT gate opening.

Knowing how other factors influence the signal-induced noise is also useful; therefore, the effect of the length of time that the high-intensity LED pulse was on and the delay time between this pulse and the gate opening were investigated. The results are depicted in figures 21 and 22. Figure 21 shows that the magnitude of SIN increases approximately linearly with increasing width of the saturating LED pulse. This result is to be expected since the longer the LED is on the more electrons are generated at the photocathode; thus, SIN is increased when the PMT gate opens.

On the other hand, for a fixed LED saturation pulse the PMT SIN decreases exponentially when the time delay between when the LED pulse turned off and the gate opened was increased, as observed in figure 22. During this measurement, the pulse width of the LED was 20 μs , its intensity level was 10 times the

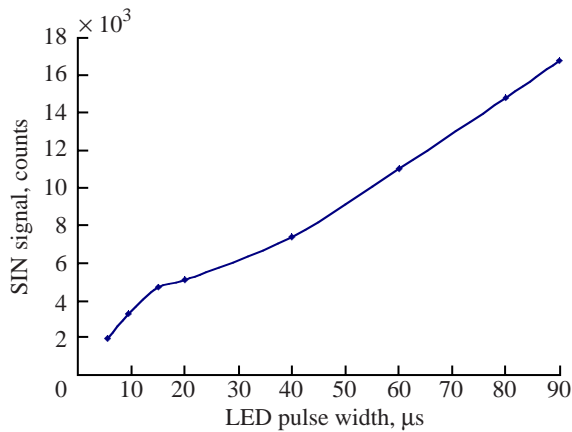


Figure 21. Correlation between signal-induced noise and LED pulse width.

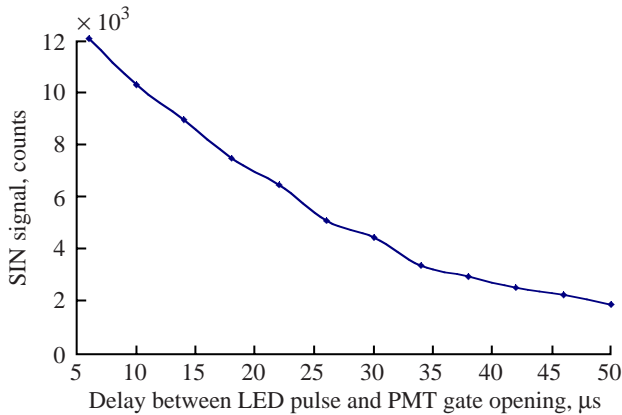


Figure 22. Correlation between SIN and time interval between LED and gate opening.

PMT saturation level, and the time constant for the decay was found to be 22.9 μs . Measurements of the decay constant of SIN were also conducted by D. Harper and DeYoung (ref. 15) with a result of 35 μs . This decay represents the loss of photocathode SIN electrons within the cathode to first dynode space by unknown mechanisms. Because of this exponential decay, waiting as long as possible before opening the PMT gate in lidar systems is advantageous.

Knowing how the mesh electrode pulse should be correlated in time with the LED 1 saturation pulse is important. For this purpose, experiments were done where the area overlap between the mesh electrode pulse and the saturating LED 1 pulse was gradually increased and the resulting SIN signal was recorded. The results are displayed in figure 23 and show a nearly linear decrease of the SIN with increasing area overlap. For optimum SIN reduction, a 100-percent area overlap should be provided; that is, the mesh electrode pulse should totally cover the saturating LED 1 pulse in time.

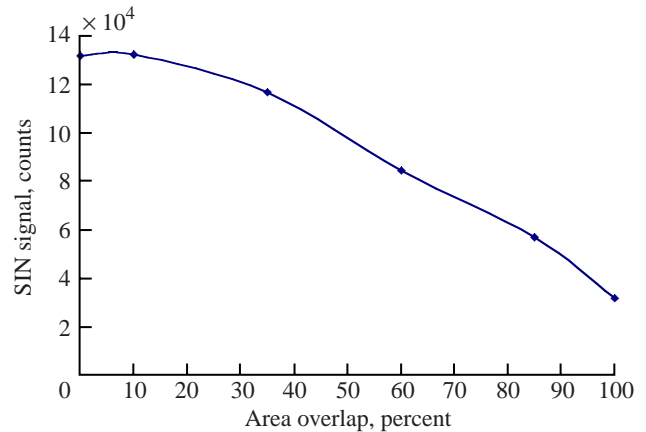


Figure 23. Effect of area overlap between mesh electrode pulse and saturating LED 1 pulse on signal-induced noise.

4.2. Mesh Voltage Effect on Simulated Lidar Signal

One of the main concerns of the mesh voltage SIN reduction method is that it should not change the actual lidar return decay signal; only the signal-induced noise should be reduced. One way to make sure that this is done is to simulate a lidar return signal with the experimental setup of figure 14, where LED 2 is pulsed with an exponential decaying signal with a specific time constant. This voltage signal is

applied to the voltage on the mesh electrode to see if there is a change in the measured time constant. In the timing diagram of figure 15, the time interval Δt between the mesh electrode pulse and the gate opening is 10 μs , whereas the pulse width for the mesh electrode is 20 μs . Three sets of measurements were taken, each 60 s long, with the mesh electrode having a magnitude of 0, 60, and 150 V; the results can be seen in figure 24. This is a logarithmic graph where the computer program has linearly fit the simulated lidar returns and the decay constants were available.

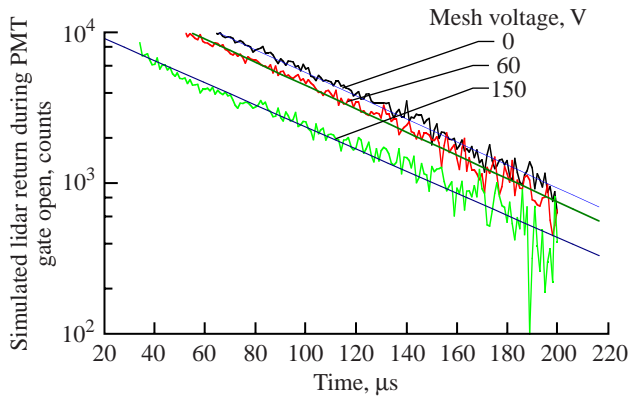


Figure 24. LED 2 simulated lidar return signals during PMT gate open time with variable mesh electrode voltage.

The mesh voltage clearly affects the amplitude of the simulated lidar signal returns, but since the DIAL equation (eq. (9)) uses a ratio between the signals, only the change in decay constant is important. Table 1 shows the LED 2 decay constant, the amplitude for the three different cases, and displays the change relative to mesh voltage of zero.

One has also to take into consideration that the error in the program to calculate the decay constants can be up to 2.2 percent. This error implies that the

Table 1. Changes in Amplitude and Decay Constant of Simulated Lidar Return Signals With Different Voltages Applied on Mesh

Mesh voltage, V	Decay constant, μs	Relative decay change, percent	Amplitude counts	Relative amplitude change, percent
0	131	0	16746	0
60	130	-0.9	14058	-16
150	137	4.1	8541	-49

slight change in the decay constant when the potential on the mesh electrode was 60 V is below the 2.2-percent limit and therefore has to be considered negligible. According to the results of figure 19, the SIN reduction is basically constant for mesh voltages higher than 60 V. We can thus draw the conclusion that as long as the mesh voltage does not exceed 60 V, the decay constant of the simulated lidar return signals (LED 2) does not change. This conclusion has important implications for lidar systems because no corruption of the lidar return occurs for mesh voltages around 60 V. Higher voltages appear to distort the internal PMT electric fields to such a degree that the PMT cannot recover in sufficient time and the lidar return signal is thus altered.

4.3. Mesh Voltage Effect on Simulated Lidar Signal With Addition of SIN

The next experiments combined a simulated lidar return signal with signal-induced noise. For this purpose, the experimental setup in figure 14 was used with both LED 1 and LED 2 active and the corresponding timing diagram in figure 15. The length of the mesh electrode pulse and the superimposed LED 1 pulse was 20 μs and the time interval between the end of the mesh pulse and the beginning of the PMT gate opening was 10 μs . By changing the neutral density filter in front of LED 1 two different saturating levels were realized: 1 times and 10 times the saturation level of the PMT. The two signals add and the result is the measured signal during opened PMT gate time. Since the SIN decays much slower than the LED 2 lidar return, a high SIN amplitude will alter the lidar return decay constant. The purpose of the experiment is to find out for which mesh voltages the decay constant of the measured signal is nearly the same as if no SIN were present.

First, measurements were taken to find the decay constant of the simulated lidar return signal (LED 2) when no signal-induced noise was present; that is, LED 1 was turned off. Since the measurements were taken on two occasions, we have two different decay constants for the PMT saturation levels. Next, LED 1 was activated and the mesh voltage potential was gradually increased, and the decay constant of the PMT output was again measured. This time the PMT signal was composed of a combination of the simulated lidar return and the SIN. According to our

theory, the mesh voltage should only decrease the SIN; thus, the decay constant for the total signal was allowed to approach the decay constant of the pure lidar return (LED 2).

The results are displayed in figure 25, and clearly the effect of the mesh voltage is different for the two LED 1 saturation levels. In the first case, when the amplitude of LED 1 just saturated the PMT, the best effect was reached between 35 and 85 V, where the decay constant of the combined lidar and SIN signal was very close to that when no SIN was present. In the second case, when the saturation level was 10 times higher, the best result was reached when the mesh electrode potential was between 30 and 50 V.

4.4. Effect of Mesh Electrode Voltage on Atmospheric Ozone Lidar Returns

Actual lidar measurements were taken, and the effect of the mesh potential was examined. In section 4.3 the conclusion was that an ideal voltage on the mesh electrode would be about 60 V. To test this conclusion, tropospheric ozone measurements were conducted with no voltage on the mesh and with 60 V on the mesh, on November 30, 1998, at 8 p.m. at the Langley Research Center. These results were compared with ozonesonde data taken at the Wallops Flight Facility on December 2, 1998, at 9 a.m., which gives a 37-hr time difference. The location of Wallops is about 95 km from the Langley Research Center, which together with the time difference will naturally produce a discrepancy in the two measurements, although at high altitudes it should be small.

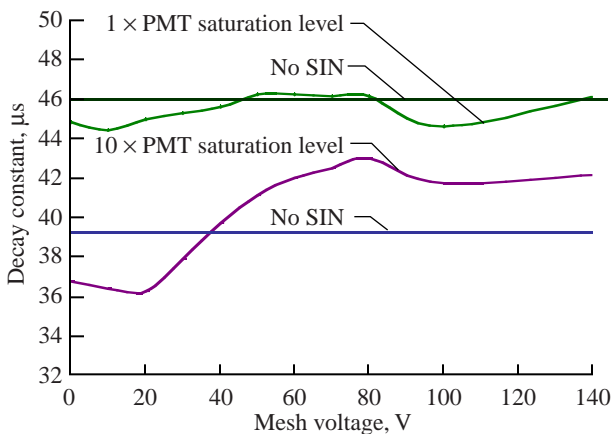


Figure 25. Effect of mesh potential on decay constant of combined simulated lidar return and SIN signal for two different PMT saturation levels.

Figure 26 displays the ozone number density as a function of altitude at the two locations. Clearly the curve that shows the measurement with 60 V on the mesh electrode is a better fit to the Wallops data compared with the data when no voltage was applied on the mesh electrode. The signal from the measurement when no voltage was applied to the mesh is heavily oscillating for low altitudes. The reason might be because the PMT is coming out of saturation from the strong near-field lidar return. Applying 60 V to the mesh electrode clearly neutralizes the oscillating effect and gives significantly better results for altitudes between 6 and 10 km. Because tropospheric wavelengths are used (289 and 299 nm for the on- and off-lines), the lidar signal level dies at altitudes above 17 km, resulting in the inability to measure ozone. It has been observed though that when voltage was applied to the mesh electrode, the ozone could be measured to slightly higher altitudes.

Although from figure 26, the measurement with 60 V on the mesh electrode gives much better values than when no voltage was applied, it is hard to say how much better it is. Therefore, defining two new parameters is convenient.

At a given altitude, the error in the ozone number density is given by the difference between the Wallops data and the Langley data, if the ozonesonde data are to be taken as the most accurate. To get an error value the measurement difference has to be divided by the Wallops value as follows:

$$(\text{Percent error})_{\text{km}} = \frac{|\text{Langley} - \text{Wallops}|}{\text{Wallops}} \quad (12)$$

An even better picture is given if the percent total error per kilometer is considered as being an average error per kilometer for a measurement up to a certain altitude:

$$\frac{\text{Percent total error}}{\text{Kilometer}} = \frac{\sum (\text{Percent error})_{\text{km}}}{\text{Altitude}} \quad (13)$$

The results from equation (13) are presented in figure 27 (the results being obtained from data in figure 26) and give a qualitative representation of the advantage of using a mesh electrode. For measurements up to 23 km, the data taken with a potential on the mesh electrode are at least 40 percent better than the data without the potential. For lower altitudes the difference can be as much as 140 percent!

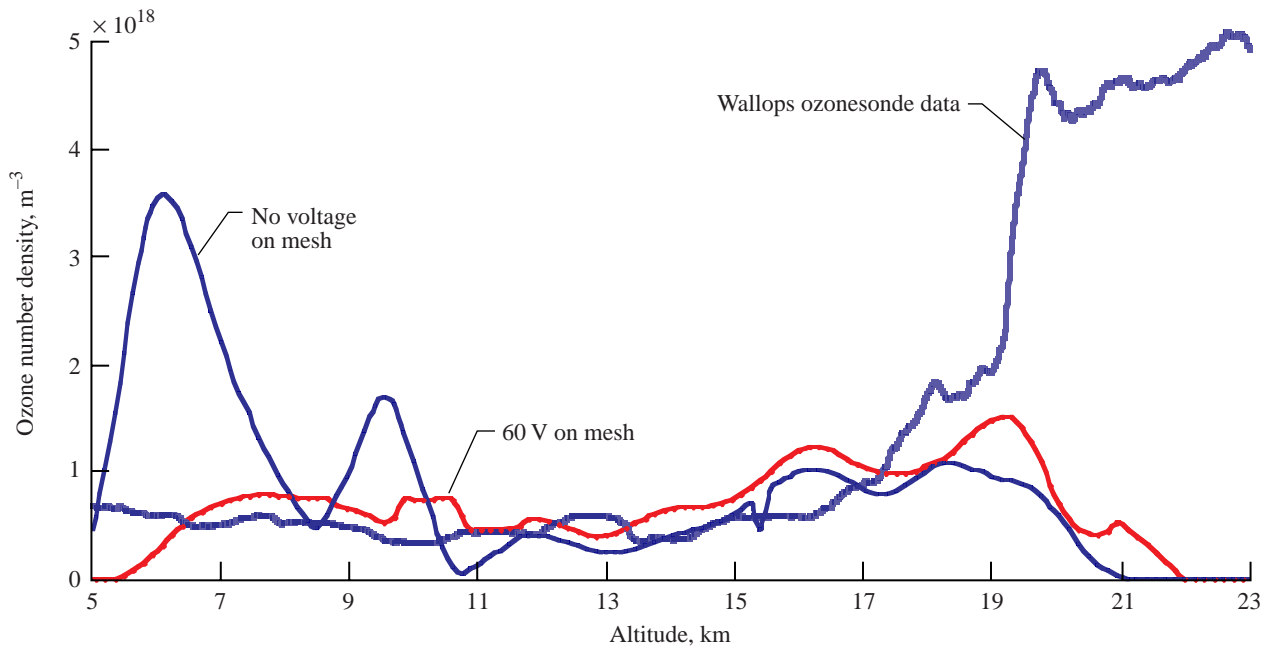


Figure 26. Comparison between ozone data from Wallops ozonesonde and ground-based tropospheric measurements conducted at Langley Research Center.

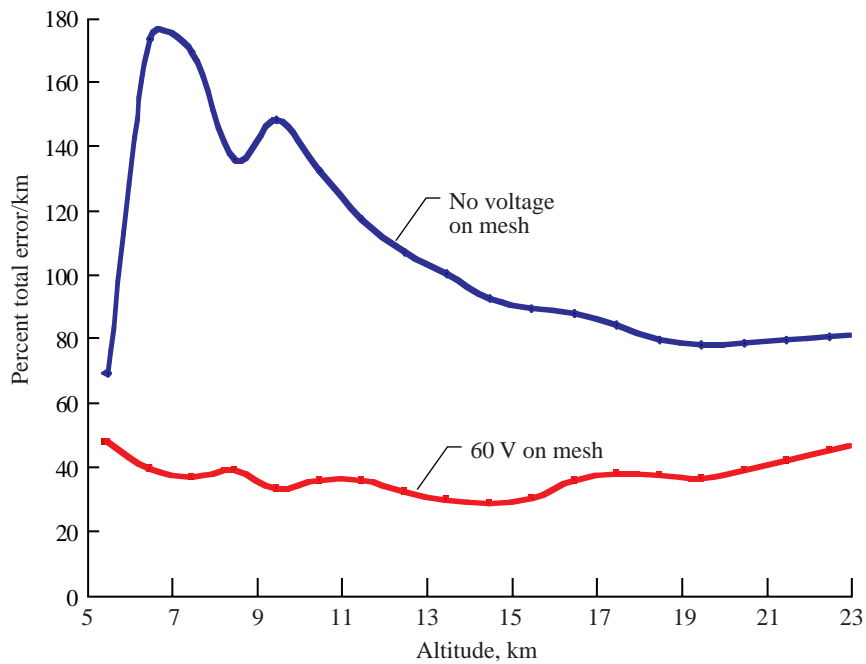


Figure 27. Effect of mesh voltage on actual lidar return signal for tropospheric measurements.

From this and other experiments conducted with actual lidar returns, the conclusion can be drawn that the reduction of the SIN due to the mesh voltage is dependent on the level of PMT saturation. Measure-

ments where the near-field return was very strong or when a cloudy sky caused high-intensity reflections heavily saturating the PMT, the effect of the mesh electrode was minimal when the voltage applied was

60 V. Because of lack of time, no experiments were conducted with different voltages on the mesh electrode at high PMT saturation levels.

Another problem that occurred during these experiments was the difficulty of measuring the saturation level of the PMT. During the simulated signal experiments, changing the voltage across the LED's varied the incoming light intensity. During actual lidar measurements, there was no way of measuring the incoming light intensity to the photocathode. Therefore, for future research, a way should be found to determine the lidar return light intensity and the related PMT saturation level. Also, the relation between the saturation level of the PMT and ideal mesh voltages should be further investigated.

5. Concluding Remarks

Signal-induced noise (SIN) is a signal generated in photomultiplier tubes (PMT's) when the photocathode receives a short intense light pulse. The photocathode creates electrons that can charge up surrounding insulators or other surfaces. At a later time, when the PMT gate opens, these electrons can be amplified by the dynode chain creating signal-induced noise. This noise signal has been shown to corrupt ozone differential absorption lidar (DIAL) measurements. This report shows a new method that could be used in lidar systems to reduce signal-induced noise in PMT detectors.

An experiment was setup to generate signal-induced noise in the PMT. A light-emitting diode (LED) was pulsed to saturate the PMT and when the PMT gate was opened at a later time, an induced noise signal was observed. Results show that SIN is a linear function of the saturation LED light pulse width and that the delay between the saturation light signal and the gate opening should be as long as possible for lower SIN levels because the SIN decreases exponentially.

A mesh electrode that could be electrically pulsed was placed in front of but external to the PMT photocathode. This electrode could alter the PMT internal electric field between the photocathode and the first dynode attracting unwanted electrons back to the photocathode; thus, signal-induced noise was reduced. The highest SIN reduction (20 percent of the no elec-

trode voltage value) was obtained when a 60-V mesh electrode pulse totally overlapped the saturating LED pulse in time.

Experiments with simulated lidar return signals (exponentially decaying LED) show that the decay time constant change due to the applied mesh electrode voltage is negligible. Ozone number densities are calculated by the DIAL equation that uses a ratio of the on and off lidar return signals; the decay time constants of the return signals are thus very important for accurate ozone number density measurements.

A saturating LED signal was added to the simulated lidar return signal and the optimum mesh voltage was shown to be around 60 V for low saturation levels ($1 \times$ PMT saturation level) and around 40 V for higher saturation levels ($10 \times$ PMT saturation level). The reduction of SIN due to the mesh voltage is thus dependent on the saturation level of the PMT.

Measurements were taken with actual lidar returns and the results were compared with ozonesonde data. The conclusion was drawn that the average total error per kilometer for ozone number densities taken with 60 V on the mesh electrode was at least 40 percent better than measurements taken with no voltage on the mesh electrode for low PMT saturation levels due to near-field returns.

The SIN reduction technique used in this report is an inexpensive and easily implemented method since it only requires a pulsed voltage source and a mesh and was shown to significantly improve ozone number density data taken with lidar receiver systems.

Future research should focus on the optimum mesh voltage for different PMT saturation levels. Thus a method should be developed to easily measure and control the saturation level of a PMT when actual lidar measurements are taken.

6. References

1. Sparling, Brien: *Stratospheric Ozone Depletion*. Numerical Aerospace Simulation Facility at NASA Ames Research Center, Updated Jan. 11, 1999. <http://science.nas.nasa.gov/Services/Education/Resources/TeacherWork/Ozone/Ozone.homepage.html> Accessed June 9, 1999.

2. *Scientific Assessment of Ozone Depletion, 1994*. National Oceanic & Atmospheric Admin., National Aeronautics & Space Admin., United Nations Environment Programme, and World Meteorological Org., 1994.
3. Albritton, Daniel L.; Monastersky, Richard; Eddy, John; Hall, J. Michael; and Shea, Eileen: *Our Ozone Shield*. NOAA Office of Global Programs. Updated Apr. 16, 1997. <http://www.ogp.noaa.gov/OGPFront/mono2.html> Accessed June 9, 1999.
4. EPA Stratospheric Protection Division: *The Science of Ozone Depletion*. Ozone Depletion. Updated June 10, 1998. <http://www.epa.gov/ozone/science> Accessed June 9, 1999.
5. Madronich, S.; and De Gruijl, F. R.: Skin Cancer and UV Radiation. *Nature*, vol. 366, no. 6450, Nov. 1993, p. 23.
6. Tevini, M., ed.: *UV-B Radiation and Ozone Depletion: Effects on Humans, Animals, Plants, Microorganisms, and Materials*. Lewis Publ., 1993.
7. Fishman, Jack; and Kalish, Robert: *Global Alert: The Ozone Pollution Crisis*. Plenum Press, 1990.
8. *Greenpeace's International Campaign To Save the Climate*. Greenpeace Org. Updated Feb. 4, 1999. <http://www.greenpeace.org/~climate/> Accessed June 9, 1999.
9. *CIESIN Thematic Guides*. CIESIN—Consortium for International Earth Science Information Network. Updated Apr. 13, 1998. <http://www.ciesin.org/TG/OZ/overview.html> Accessed June 9, 1999.
10. Heck, Walter W.; Cure, William W.; Rawlings, John O.; Zaragoza, Lawrence J.; Heagle, Allen S.; Heggestad, Howard E.; Kohut, Robert J.; Kress, Lance W.; and Temple, Patrick J.: Assessing Impacts of Ozone on Agricultural Crops—1: Overview. *J. Air Pollut. Control Assoc.*, vol. 34, no. 7, 1984, pp. 725–735.
11. Ollinger, S. V.; Aber, J. D.; and Reich, P. B.: Simulating Ozone Effects on Forest Productivity. *Ecolog. Appl.*, vol. 7, Jan. 1997, pp. 1237–1254.
12. Lippmann, Morton: Health Effects of Ozone: A Critical Review. *J. Air Pollut. Control Assoc.*, vol. 39, no. 5, 1989, pp. 672–695.
13. Browell, E. V.; Butler, C. F.; Kooi, S. A.; Fenn, M. A.; and Harriss, R. C.: Large-Scale Variability of Ozone and Aerosols in the Summertime Arctic and Subarctic Troposphere. *J. Geophys. Res.*, vol. 97, No. D15, Oct. 1992, pp. 16433–16450.
14. Browell, E. V.; Butler, C. F.; Fenn, M. A.; Grant, W. B.; and Ismail, S.: Ozone and Aerosol Changes During the 1991–1992 Airborne Arctic Stratospheric Expedition. *Science*, vol. 261, no. 5125, Aug. 1993, pp. 1155–1158.
15. Harper, David B.; and DeYoung, Russell J.: *Signal-Induced Noise Effects in a Photon Counting System for Stratospheric Ozone Measurement*. NASA/TM-1998-204674, 1998.
16. McDermid, I. S.; Godin, S. M.; et al.: Comparison of Ozone Profiles From Ground-Based Lidar, ECC Balloon Sonde, ROCOZ-A Rocket Sonde, and SAGE-2 Satellite Measurements. *J. Geophys. Res.*, vol. 95, 1990, pp. 10037–10042.
17. Proffitt, M. H.; and Langford, A. O.: Ground Based Differential Lidar System for Day or Night Measurement of Ozone Throughout the Free Troposphere. *Appl. Opt.*, vol. 36, 1997, pp. 2568–2585.
18. Williamson, C. K.; and DeYoung, R. J.: Reduction of PMT Signal-Induced Noise in Lidar Receivers. *Nineteenth International Laser Radar Conference*. Upendra N. Singh, Syed Ismail, and Geary K. Schwemmer, eds., NASA/CP-1998-207671/PT2, 1998, pp. 751–754.
19. Measures, Raymond M.: *Laser Remote Sensing: Fundamentals and Applications*. John Wiley and Son, 1984.
20. Proffitt, M. H.; and Langford, A. O.: Profiling of Ozone in the Free Troposphere by the Lidar Technique. *Rev. Laser Eng.*, vol. 23, no. 2, 1995, pp. 104–107.
21. Edner, H.; Faris, G. H.; et al.: Mobile Remote Sensing System for Atmospheric Monitoring, *Appl. Opt.*, vol. 26, 1996, pp. 4330–4338.
22. Browell, E. V.; Ismail, S.; and Grant, W. B.: Differential Absorption Lidar (DIAL) Measurements From Air and Space. *Appl. Phys. B: Lasers & Opt.*, vol. 67, 1998, pp. 399–410.
23. *Photomultiplier Tubes*. HAMAMATUSU—The Photon Is Our Business. Updated June 9, 1999. <http://optics.org/hamamatsu/pmt.html> Accessed June 9, 1999.
24. Dereniak, Eustace L.; and Crowe, Devon G.: *Optical Radiation Detectors*. John Wiley & Sons, Inc., 1984.
25. Sommer, A. H.: *Photoemissive Materials*. Robert E. Krieger Pub. Co., 1980.
26. Engstrom, Ralph W.: *Photomultiplier Handbook*. RCA Corp., 1980.
27. Hidehiro, Kume: *Photomultiplier Tube: Principle to Application*. Hamamatsu Photonics, 1994.
28. Hunt, W. H.; and Poultney, S. K.: Testing the Linearity of Response of Gated Photomultipliers in Wide Dynamic Range Laser Radar Systems. *IEEE Trans. Nucl. Sci.*, vol. NS-22, no. 1, Feb. 1975, pp. 116–120.

29. Charpak, G.: Retardation Effects Due to the Localized Application of Electric Fields on the Photocathode of a Photomultiplier. *Nucl. Instr. & Methods*, vol. 51, 1967, pp. 125–128.
30. Dahl, David A.: SIMION 3D, Version 6.0. *ASMA Conference on Mass Spectrometry and Allied Topics*, May 1995, p. 717.
31. Browell, E. V.; Carter, A. F.; Shipley, S. T.; Allen, R. J.; Butler, C. F.; Mayo, M. N.; Siviter, J. H., Jr.; and Hall, W. M.: The NASA Multipurpose Airborne DIAL System and Measurements of Ozone and Aerosol Profiles. *Appl. Opt.*, vol. 22, no. 4, Feb. 1983, pp. 522–534.
32. *Photomultipliers, and Accessories Catalog*. Electron Tubes Ltd., 1996.
33. Harper, D. B.: Fiber-Optic Coupled Lidar Receiver System To Measure Stratospheric Ozone. MS Thesis, Old Dominion University, Dec. 1988.

REPORT DOCUMENTATION PAGE

Form Approved
OMB No. 0704-0188

Public reporting burden for this collection of information is estimated to average 1 hour per response, including the time for reviewing instructions, searching existing data sources, gathering and maintaining the data needed, and completing and reviewing the collection of information. Send comments regarding this burden estimate or any other aspect of this collection of information, including suggestions for reducing this burden, to Washington Headquarters Services, Directorate for Information Operations and Reports, 1215 Jefferson Davis Highway, Suite 1204, Arlington, VA 22202-4302, and to the Office of Management and Budget, Paperwork Reduction Project (0704-0188), Washington, DC 20503.

1. AGENCY USE ONLY (Leave blank)	2. REPORT DATE January 2000	3. REPORT TYPE AND DATES COVERED Technical Memorandum	
4. TITLE AND SUBTITLE A New Method for Reduction of Photomultiplier Signal-Induced Noise		5. FUNDING NUMBERS WU 274-00-99-24	
6. AUTHOR(S) Andrea Koble and Russell DeYoung			
7. PERFORMING ORGANIZATION NAME(S) AND ADDRESS(ES) NASA Langley Research Center Hampton, VA 23681-2199		8. PERFORMING ORGANIZATION REPORT NUMBER L-17843	
9. SPONSORING/MONITORING AGENCY NAME(S) AND ADDRESS(ES) National Aeronautics and Space Administration Washington, DC 20546-0001		10. SPONSORING/MONITORING AGENCY REPORT NUMBER NASA/TM-2000-209836	
11. SUPPLEMENTARY NOTES Koble: Lund University, Lund, Sweden; DeYoung: Langley Research Center, Hampton, VA.			
12a. DISTRIBUTION/AVAILABILITY STATEMENT Unclassified-Unlimited Subject Category 74 Availability: NASA CASI (301) 621-0390		12b. DISTRIBUTION CODE	
13. ABSTRACT (Maximum 200 words) For lidar measurements of ozone, photomultiplier tube (PMT) detector signal-induced noise represents a fundamental problem that complicates the extraction of information from lidar data. A new method is developed to significantly reduce signal-induced noise in lidar receiver PMT detectors. The electron optics of the lidar photomultiplier detector is modified to filter the source of signal-induced noise. A mesh electrode external to the PMT is utilized to control photoemission and disorient electron trajectories from the photocathode to the first dynode. Experiments were taken both with simulated and actual lidar return signals at Langley Research Center. Results show at least 40 percent more accurate ozone number density values with a mesh voltage of 60 V applied than with no voltage applied.			
14. SUBJECT TERMS Signal-induced noise; PMT noise; Lidar		15. NUMBER OF PAGES 27	
		16. PRICE CODE A03	
17. SECURITY CLASSIFICATION OF REPORT Unclassified	18. SECURITY CLASSIFICATION OF THIS PAGE Unclassified	19. SECURITY CLASSIFICATION OF ABSTRACT Unclassified	20. LIMITATION OF ABSTRACT UL